

Villapún VM, Zhang H, Howden C, Cheung Chow L, Esat F, Pérez P, Sort J, Bull S, Stach J, González S.

[Antimicrobial and wear performance of Cu-Zr-Al metallic glass composites.](#)

*Materials and Design* 2016

DOI: <http://dx.doi.org/10.1016/j.matdes.2016.11.029>

**Copyright:**

© 2016. This manuscript version is made available under the [CC-BY-NC-ND 4.0 license](#)

**DOI link to article:**

<http://dx.doi.org/10.1016/j.matdes.2016.11.029>

**Date deposited:**

17/11/2016

**Embargo release date:**

10 November 2017



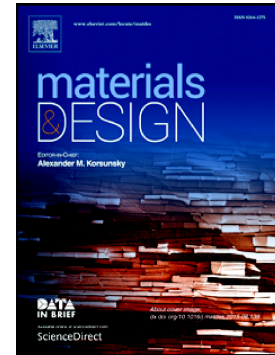
This work is licensed under a

[Creative Commons Attribution-NonCommercial-NoDerivatives 4.0 International licence](#)

## Accepted Manuscript

Antimicrobial and wear performance of Cu-Zr-Al metallic glass composites

Victor M. Villapún, H. Zhang, C. Howden, L. Cheung Chow, F. Esat, P. Pérez, J. Sort, S. Bull, J. Stach, S. González



PII: S0264-1275(16)31409-5  
DOI: doi: [10.1016/j.matdes.2016.11.029](https://doi.org/10.1016/j.matdes.2016.11.029)  
Reference: JMADE 2465

To appear in: *Materials & Design*

Received date: 24 September 2016  
Revised date: 3 November 2016  
Accepted date: 4 November 2016

Please cite this article as: Victor M. Villapún, H. Zhang, C. Howden, L. Cheung Chow, F. Esat, P. Pérez, J. Sort, S. Bull, J. Stach, S. González, Antimicrobial and wear performance of Cu-Zr-Al metallic glass composites. The address for the corresponding author was captured as affiliation for all authors. Please check if appropriate. Jmade(2016), doi: [10.1016/j.matdes.2016.11.029](https://doi.org/10.1016/j.matdes.2016.11.029)

This is a PDF file of an unedited manuscript that has been accepted for publication. As a service to our customers we are providing this early version of the manuscript. The manuscript will undergo copyediting, typesetting, and review of the resulting proof before it is published in its final form. Please note that during the production process errors may be discovered which could affect the content, and all legal disclaimers that apply to the journal pertain.

# Antimicrobial and wear performance of Cu-Zr-Al metallic glass composites

Victor M. Villapún<sup>a</sup>, H. Zhang<sup>b</sup>, C. Howden<sup>g</sup>, L. Cheung Chow<sup>g</sup>, F. Esat<sup>c</sup>, P. Pérez<sup>d</sup>, J. Sort<sup>b,e</sup>,  
S. Bull<sup>f</sup>, J. Stach<sup>g</sup>, S. González<sup>a,\*</sup>

<sup>a</sup>Faculty of Engineering and Environment, Northumbria University, Newcastle upon Tyne NE1 8ST, UK

<sup>b</sup>Departament de Física, Facultat de Ciències, Universitat Autònoma de Barcelona, E-08193 Bellaterra, Spain

<sup>c</sup>Institute for Materials Research. University of Leeds, Leeds, LS2 9JT, UK

<sup>d</sup>Centro Nacional de Investigaciones Metalúrgicas, CSIC, Avda. Gregorio del Amo 8, 28040 Madrid, Spain

<sup>e</sup>Institució Catalana de Recerca i Estudis Avançats (ICREA), Pg. Lluís Companys 23, 08010 Barcelona, Spain

<sup>f</sup>Newcastle University, School of Chemical Engineering and Advanced Materials, Newcastle upon Tyne NE1 7RU, UK

<sup>g</sup>Newcastle University, School of Biology, Newcastle upon Tyne NE1 7RU, UK

Keywords: Tribological properties; Antimicrobial behaviour; Metallic glass composite; Scratch test; Nanoindentation

\*Corresponding author. Tel.: +44 (0) 191 349 5937

E-mail address: sergio.sanchez@northumbria.ac.uk (S. González)

## Abstract

The antimicrobial and wear behaviour of metallic glass composites corresponding to the  $\text{Cu}_{50+x}(\text{Zr}_{44}\text{Al}_6)_{50-x}$  system with  $x=(0, 3 \text{ and } 6)$  has been studied. The three compositions consist of crystalline phases embedded in an amorphous matrix and they exhibit crystallinity increase with increasing Cu content, i.e., decrease of the glass-forming ability. The wear resistance also increases with the addition of Cu as indirectly assessed from  $H/E_r$  and  $H^3/E_r^2$  parameters obtained from nanoindentation tests. These results are in agreement with scratch tests since for the alloy with highest Cu content, i.e.,  $\text{Cu}_{56}\text{Zr}_{38.7}\text{Al}_{5.3}$ , reveals a crack increase, lower pile-up, prone adhesion wear in dry sliding and higher scratch groove volume to pile-up volume. Samples with higher Cu content revealed higher hydrophilicity. Time-kill studies revealed higher reduction in colony-forming units for *E. coli* (gram-negative) and *B. subtilis* (gram-positive) after 60 min of contact time for the  $\text{Cu}_{56}\text{Zr}_{38.7}\text{Al}_{5.3}$  alloy and all the samples achieved a complete elimination of bacteria in 250 min.

## 1. Introduction

Nosocomial infections (i.e., hospital-acquired infections, HAI) and bacterial resistance to antibiotics are topics of utmost importance in [1]. For this reason, numerous studies about the economic and social impact of HAI have been performed over the years [2-4]. For example, a European survey from 2011–2012 estimated that the total annual number of patients with HAI in European acute care hospitals was 3.2 million [5]. The most common method to tackle this challenge in hospitals is to clean touch surfaces using chemical products. The major drawback is that the large number of touch surfaces requires considerable financial resources to ensure proper surface sterilization. In this regard, the self-sterilizing behaviour of antimicrobial materials makes them an appealing alternative to tackle this issue. Among these materials, Cu is the most frequently used due to its efficiency in “contact killing” and therefore it has been used for multiple applications in healthcare [6]. The mechanisms behind the antimicrobial activity of Cu are not completely understood yet but it is commonly accepted that the release of ions from the surface plays an important role in this effect.

Most of the studies carried out over the years have focused on using Cu and Cu alloys in the crystalline state. The major drawbacks for using these materials are their relatively low hardness and low wear resistance. These properties can be increased when the alloys are in an amorphous/crystalline state (i.e., metallic glass composites) [7, 8]. This can be accomplished by developing new alloys with increased glass forming ability (GFA) through alloying Cu with other elements, especially with Zr and Al. However, addition of such elements may result in losing part of the antimicrobial ability when these elements are non-antimicrobial.

Bulk metallic glasses (BMGs) exhibit higher yield strength and lower Young's modulus than their crystalline counterparts resulting in higher wear resistance [8]. This has triggered a growing interest in designing novel Cu-based BMGs [9] as touch surfaces. Despite the interest in the topic, the number of studies dealing with the antimicrobial behaviour of BMGs is still very small. For example, Huang et al. [10] studied the antimicrobial effect against the Gram positive bacterium *S. aureus* of Cu-containing Zr-based BMGs. The authors concluded that the number of colony forming units (CFU) on Zr-based BMGs after 4 h of moist contact was about one order of magnitude lower than on Ti-6Al-4V alloy. From the point of view of the tribological behaviour of metallic glasses, there are numerous studies about the interaction of a cylindrical sample and a surface (pin-on disc) or the interaction between a diamond tip and the surface (scratch test) when the material is either in bulk shape or as thin film [8, 9, 11-14]. However, studies dealing with the ability to tune the wear resistance of BMG composites by controlling the formation of intermetallic phases are scarce.

The aim of this study is to control the composition of Cu-rich BMG composites corresponding to the Cu-Zr-Al system to tune the volume fraction of the crystalline phase in order to optimize the wear resistance and antimicrobial behaviour. For alloys of the Cu-Zr-Al system, the strength and hardness is highest in a partly crystalline state [15]. According to Inoue et al. [15], for this alloy

system, the hardness increases with increasing volume fraction of crystalline phase up to a maximum critical value beyond which it drops. We have therefore explored in this work composites with similar volume fraction of crystalline phase to tune the mechanical performance.

Regarding the antimicrobial behaviour, the performance of Cu is reported to be attributed to the release of  $\text{Cu}^+$  and  $\text{Cu}^{++}$  ions, which is favoured by the presence of ion diffusion paths, such as grain boundaries, dislocations, etc [16]. The lack of grain boundaries and dislocations in amorphous materials does not make them good candidate antimicrobial materials. However, using rapid solidification to favour the formation of fine microstructures (ion diffusion paths) generally promotes the antimicrobial behaviour, which also explains the interest in developing BMG composites with high volume fraction of crystalline phase. Despite alloys corresponding to the Cu-Zr system with Cu/Zr ratio of 1.5, such as  $\text{Cu}_{50}\text{Zr}_{43}\text{Al}_7$  (at. %), exhibit rather high GFA [17], it is also true that their GFA is very composition sensitive, i.e., alloys with similar composition exhibit very different GFA [18]. This can result in alloys of different degrees of amorphicity even for similar composition and therefore could have large effect on the mechanical behaviour [19], which is in agreement with our results obtained using nanoindentation and scratch tests. The antimicrobial studies of this work have been performed using Gram-positive and Gram-negative bacteria since both types of bacteria can be found on touch surfaces and they exhibit different sensitivity against Cu ions [20]. Although some authors have previously studied the antimicrobial behaviour of Cu-containing metallic glasses [10, 21] the possibility of tuning the antimicrobial performance by controlling the formation of crystalline phase has been mostly overlooked.

## 2. Experimental

Alloy ingots with nominal composition  $\text{Cu}_{50+x}(\text{Zr}_{44}\text{Al}_6)_{50-x}$  with  $x=(0, 3 \text{ and } 6)$  were prepared from elements with purity higher than 99.9 at. %. The master alloys were re-melted three times in a Zr-gettered high purity argon atmosphere to attain good chemical homogeneity. Rod samples of 2 mm in diameter were obtained from the master alloy by copper mould casting in an inert gas atmosphere. The structure of the as-cast and thermally-treated samples was studied by X-ray diffraction (XRD), using a Bruker D8 diffractometer with monochromated Cu  $K\alpha$  radiation (2 $\theta$  range 20°-90°, step size = 0.03°). The microstructure was investigated with a scanning electron microscope (SEM) (Mira FEM-SEM Tescan) equipped with energy-dispersive X-ray (EDX) analysis. To identify the microstructures, at least ten EDX microanalysis were performed for each of the phases present in each of the three alloys. To evaluate the mechanical properties, cylindrical specimens with 2:1 aspect ratio were tested at room temperature under compression at a strain rate of  $2 \times 10^{-4} \text{ s}^{-1}$  in a universal Servosis machine. Nanoindentation experiments were performed at room temperature at approximately half the radius distance from the centre in a UMIS equipment from Fischer-Cripps Laboratories, in the load control mode and using a Berkovich-type diamond tip. Prior to the nanoindentation and scratch test the surfaces were mirror-like polished. From the large number of indentations performed (more than 20) and the high load applied

(300mN) we have sampled all the existing phases and obtained a statistical mean value. A Teer Coating Limited scratch tester model ST220 was used for the scratch tests of the mirror-like polished samples. The tests were performed at a load of 30 N at a stage speed of 10 mm/min. The scratched surfaces (profile and roughness) were analysed using an Alicona profilometer and the profiles were obtained averaging 5 measurements. Contact angle measurements were carried out using the sessile drop technique, with a Krüss drop size DSA30 analyser and depositing 1  $\mu$ l of deionized water at a rate of 30  $\mu$ /min.

For initial antimicrobial tests, *E. coli* strain K12 (Gram-negative) and *Bacillus subtilis* strain 168 (Gram-positive) were incubated (30°C), with shaking (200 rpm), in 25 ml of Mueller-Hinton Broth (MHB) for 16 hours. Cultures were diluted in MHB to an optical density (OD<sub>600</sub>) of 0.01. The diluted cultures were incubated at 37°C until they reached an OD<sub>600</sub> of ~ 0.3. A quantity equal to 1  $\mu$ l of the respective cultures was pipetted off directly onto the ground (4000 grit) surfaces of the specimen and control (copper and plastic) samples. Inoculated samples were placed inside a petri dish containing moist tissue, sealed and statically incubated for 4 hours at 37°C, after which they were diluted in 99  $\mu$ l of MHB. Samples were serially diluted, plated onto MH agar and resulting colonies were counted after 16 hours of incubation at 37°C. All tests were done in triplicate and mean counts reported. Time-kill experiments were done as above, but a lower initial inoculum density was used (ca.  $1 \times 10^6$  cells/ml) and cell counts were taken every hour 60 mins.

### 3. Results and discussion

#### 3.1. Microstructure

Fig. 1 shows the XRD scans of 2 mm diameter rods of  $\text{Cu}_{50+x}(\text{Zr}_{44}\text{Al}_6)_{50-x}$  ( $x=0$ ,  $x=3$  and  $x=6$ ). For the  $\text{Cu}_{50}\text{Zr}_{44}\text{Al}_6$  alloy high intensity peaks associated to orthorhombic  $\text{Cu}_{10}\text{Zr}_7$  ( $a = 0.9347$  nm,  $b = 0.9347$  nm,  $c = 1.2675$  nm), orthorhombic  $\text{Cu}_8\text{Zr}_3$  ( $a = 0.78686$  nm,  $b = 0.81467$  nm,  $c = 0.9977$  nm), B19' CuZr martensite and also probably austenite B2 CuZr are detected and superimposed on a broad halo suggesting that along with the crystalline phases an amorphous phase is present. For the  $\text{Cu}_{53}\text{Zr}_{41.4}\text{Al}_{5.6}$  alloy, the intensity of the broad halo decreases while the intensity of the XRD peaks, especially those detected at around 40°, increase. A larger number of peaks associated to  $\text{Cu}_{10}\text{Zr}_7$  and  $\text{Cu}_8\text{Zr}_3$  are also observed. Finally, for the alloy with highest content Cu content (i.e.,  $\text{Cu}_{56}\text{Zr}_{38.7}\text{Al}_{5.3}$ ), the broad halo is practically undetectable and the peaks corresponding to  $\text{Cu}_{10}\text{Zr}_7$  and  $\text{Cu}_8\text{Zr}_3$  further increase in intensity, especially the one at about 41.5°. The peaks also tend to get narrower, suggesting growth of the crystallite size and additional peaks corresponding to CuZr phases, both austenite B2 and martensite B19', are detected. These results show that, in general, the number and intensity of the XRD peaks tend to increase and the intensity of the broad halo to decrease with increasing Cu content thus suggesting a decrease in the glass forming ability (GFA). The detection of these phases is consistent with previous works on other ZrCu-based BMG composites [22-24]. The formation of the stable intermetallic phases  $\text{Cu}_{10}\text{Zr}_7$  [25],  $\text{Cu}_8\text{Zr}_3$  and CuZr

could be due to strong interaction of Cu and Zr atoms since the enthalpy of mixing ( $\Delta H_{\text{mix}}$ ) of Zr-Cu pair is -23 kJ/mol, stronger than the Cu-Al pair ( $\Delta H_{\text{mix}} = -1$  kJ/mol) [26].

To better understand the differences between the three alloy compositions, the microstructures were also investigated by scanning electron microscopy at different magnifications. Fig. 2 shows the general backscattered SEM images from the cross section of the 2 mm diameter rods of the three compositions, acquired at half the radius distance from the centre. For the  $\text{Cu}_{50}\text{Zr}_{44}\text{Al}_6$  alloy (Fig. 2a), dendrites of different sizes are observed. The brightness of the dendrites tend to get darker with increasing size and they are slightly darker than the matrix. For the alloy  $\text{Cu}_{53}\text{Zr}_{41.4}\text{Al}_{5.6}$  (Fig. 2b) the microstructure changes dramatically since most of the crystalline phases consist of large and well-developed dendrites with arms of up to 10  $\mu\text{m}$  length. However, small round crystalline phases of about 1  $\mu\text{m}$  homogeneously dispersed in the matrix and also located around the dendrites are also present. Not only the size of the dendrites have grown with increasing Cu addition, due to the decrease of the GFA, but also the surrounding clear phase associated to CuZr has grown and they follow a growth process similar to that previously observed [27]. At this stage the volume fraction of crystalline phase seems to be large enough to reach the percolation threshold (i.e., volume fraction of the crystalline phase beyond which connectivity between them first appears). The alloy with highest Cu content,  $\text{Cu}_{56}\text{Zr}_{38.7}\text{Al}_{5.3}$  (Fig. 2c) exhibits, at the half radius distance from the centre, a very similar microstructure to that of the alloy with 53 at. % Cu but the dendrites are more evolved. This confirms the decrease of the GFA with increasing Cu content. For this composition, and contrary to the alloys with 50 and 53 at. % Cu, no featureless matrix is observed and therefore it appears to be fully crystalline. At this stage, the connectivity between the crystalline phases is practically continuous. The effect of the percolation on the mechanical performance will be analysed in more detail in section 3.2.2. (scratch tests).

The volume fraction of the crystalline phases present for each composition have been estimated from Fig. 2 since these show representative microstructures. The large difference in tonality among the crystalline phases enables to estimate their volume fraction:  $\text{Cu}_{50}\text{Zr}_{44}\text{Al}_6$  (~10 % dendrites),  $\text{Cu}_{53}\text{Zr}_{41.4}\text{Al}_{5.6}$  (~15 %  $\text{Cu}_8\text{Zr}_3$ , grey particles ~5 % CuZr and white halo ~15 %  $\text{Cu}_{10}\text{Zr}_7$ ) and  $\text{Cu}_{56}\text{Zr}_{38.7}\text{Al}_{5.3}$  (~40 %  $\text{Cu}_8\text{Zr}_3$ , grey particles ~10 % CuZr and white matrix ~50 %  $\text{Cu}_{10}\text{Zr}_7$ ). The percolation threshold (i.e., the volume fraction of crystalline phase for which connectivity first appears) is close to that of the composition  $\text{Cu}_{53}\text{Zr}_{41.4}\text{Al}_{5.6}$  and therefore is consistent with the 35 % threshold previously reported [28] and this value also is within the range of 30 to 50 % observed by Pauly et al. [22].

To more clearly identify the crystalline structure of the three alloys, the microstructure at the middle radius has been observed at higher magnification (backscattered SEM images of Fig. 3). The composition (i.e., at. % Cu, Zr and Al) of the phases labelled on Fig. 3 are listed on Table 1.

For the  $\text{Cu}_{50}\text{Zr}_{44}\text{Al}_6$  alloy (Fig. 3a) dendrites of sizes ranging from less than 1  $\mu\text{m}$  up to 3  $\mu\text{m}$  homogeneously dispersed in the matrix are observed. The composition of the large dendrites (phase 2a) is  $\text{Cu}_{50.2}\text{Zr}_{35.4}\text{Al}_{14.5}$  at. %, slightly richer in Cu and poorer in Zr than the nominal

composition. The Cu/Zr ratio of the large dendrites is about 1.4, and therefore could be attributed to  $\text{Cu}_{10}\text{Zr}_7$ . The composition of the surrounding matrix, phase 1a ( $\text{Cu}_{54.3}\text{Zr}_{40}\text{Al}_{5.6}$  at. %) is closer to the nominal composition and the small differences could be mainly ascribed to the potential influence of surrounding small dendrites. These results are consistent with the XRD scans since most of the XRD peaks could be attributed to  $\text{Cu}_{10}\text{Zr}_7$ . The small intensity peaks corresponding to the CuZr phase detected in the XRD scan may be attributed to the small dendrites (compositional analysis was not performed due to their small size) and would indicate that the dendrites get enriched in Cu as they grow.

The intermediate  $\text{Cu}_{53}\text{Zr}_{41.4}\text{Al}_{5.6}$  alloy consists basically of 4 phases of different tonality (Fig. 3b). The darkest phase corresponds to the dendrites (phase 3b), which exhibits a complex microstructure that seems to consist of two very fine phases of different colour. The composition of the dendrites is  $\text{Cu}_{58.7}\text{Zr}_{32.5}\text{Al}_{8.8}$  at. %, however, no ternary intermetallic of similar composition has been reported in the literature [29]. This suggests that the composition obtained is the result of the two fine phases present in the dendrite. These phases would correspond to the intermetallics  $\text{Cu}_8\text{Zr}_3$  and  $\text{Cu}_{10}\text{Zr}_7$  detected by XRD (Fig. 1). In fact the Cu/Zr ratio for  $\text{Cu}_{58.7}\text{Zr}_{32.5}\text{Al}_{8.8}$  ( $58.7/32.5=1.79$ ) is intermediate between that of  $\text{Cu}_8\text{Zr}_3$  (2.66) and  $\text{Cu}_{10}\text{Zr}_7$  (1.43). The Al content of the dendrites (i.e., 8.8 at. %) is higher than that of the nominal composition of the alloy (i.e., 5.6 at. %) thus suggesting that it remains in solid solution. The extension of this solid solution solubility would have been promoted by the rapid cooling fabrication process [30].

Close to the dendrites there are geometric particles (phase 2b) with a composition of  $\text{Cu}_{42.5}\text{Zr}_{46.2}\text{Al}_{11.3}$  at. %. The similar content in Cu and Zr suggest that these particles correspond to CuZr, one of the phases detected by XRD. Most of the dendrites and the geometric particles are surrounded by a halo of clear tonality (phase 4b) with a composition of  $\text{Cu}_{53.5}\text{Zr}_{42.7}\text{Al}_{3.9}$  (at. %), which is poorer in Al than the nominal composition of the  $\text{Cu}_{53}\text{Zr}_{41.4}\text{Al}_{5.6}$  alloy. These results suggest that the nucleation and growth of  $\text{Cu}_8\text{Zr}_3$  and CuZr phases occur with absorption of Al from the surrounding matrix, leaving the halo poor in Al. The composition at the matrix and far from the dendrites (phase 1b) is  $\text{Cu}_{55}\text{Zr}_{39.4}\text{Al}_{5.7}$  at. %, i.e., very close to the nominal composition, suggesting that this corresponds to the amorphous matrix.

For the alloy with highest Cu content, i.e.,  $\text{Cu}_{56}\text{Zr}_{38.7}\text{Al}_{5.3}$  (Fig. 3c), the dendrites exhibit a very homogeneous dark tonality, although in some areas very small white particles are also present. The composition of the dendrites (phase 3c) according to the EDX microanalysis is  $\text{Cu}_{61.2}\text{Zr}_{28.3}\text{Al}_{10.5}$  (at. %) with a Cu/Zr ratio of about 2.16, much closer to that of  $\text{Cu}_8\text{Zr}_3$  (2.66) than to  $\text{Cu}_{10}\text{Zr}_7$  (1.43). This suggests that the volume fraction of  $\text{Cu}_8\text{Zr}_3$  phase inside the dendrites is higher than that of  $\text{Cu}_{10}\text{Zr}_7$  phase. The results also show that the dendrites get richer in Cu with increasing content in Cu of the alloy. The geometric particles of grey colour (phase 2c) have similar content in Cu and Zr and therefore they can be associated to CuZr. All these particles are embedded in a matrix (phase 1c) with composition  $\text{Cu}_{55.3}\text{Zr}_{42.3}\text{Al}_{2.4}$  (at. %), similar to the composition of the halo present in the alloy containing 53 at. % Cu and could be attributed to  $\text{Cu}_{10}\text{Zr}_7$ . These phases detected are similar to those observed by Yokoyama et al. [31] for alloys corresponding to the ZrCuAl system.



These results suggest that as the GFA decreases with increasing Cu content, the halo surrounding the dendrites expand until they collide and constitute the matrix. Finally, very dark spots distributed mostly at the grain boundaries and interfaces are observed. These spots would correspond to holes because according to the microanalysis no difference in composition with the surrounding matrix could be detected. For all the compositions, the results from microanalysis are consistent with differences in atomic weight of the elements (Cu: 63.546, Zr:91.224 and Al:26.9815) [32] where a brighter backscattered image indicates a higher concentration of high atomic weight elements. The order from brightest to darkest is thus:  $Zr_1/Cu_1$  ( $Cu_1Zr_1$ ) >  $Zr_7/Cu_{10}$  ( $Cu_{10}Zr_7$ ) >  $Zr_3/Cu_8$  ( $Cu_8Zr_3$ ).

### 3.2. Mechanical behaviour

The mechanical behaviour of the alloys with 50, 53 and 56 at. % Cu were initially evaluated from compression tests. All the compositions were found to be brittle (i.e., the samples fractured in the elastic region) and therefore probably failed before the yield stress was reached (data not shown). Multiple step drops were detected in the elastic region upon loading, indicating the presence of internal flaws, probably porosity. This suggests that uniaxial compression is not a good technique to measure certain mechanical properties of these materials and therefore a more local technique where small sample volumes are involved in the deformation, was required. Nanoindentation is an excellent technique in such circumstances [33]. Furthermore, the wear resistance was assessed using scratch testing to compare the performance of the different alloys.

#### 3.2.1. Nanoindentation tests

The mechanical behaviour of the three different investigated compositions was characterized by nanoindentation with a maximum load of 300 mN, large enough to sample all the crystalline phases and get average values of the different mechanical properties. Fig. 4 shows representative load-displacement (P-h) curves obtained at half the radius of the disk's cross-section. The maximum displacement  $h_{max}$  decreases with increasing the Cu content from  $h_{max}=1.485\ \mu m$  for  $Cu_{50}Zr_{44}Al_6$  to  $1.372\ \mu m$  for  $Cu_{56}Zr_{38.7}Al_{5.3}$ . This can be ascribed to the increasing volume fraction of brittle and mechanically hard intermetallic phases. Remarkably, clear pop-in events are observed for the samples containing an amorphous fraction (i.e., 50 at.% and 53 at.% Cu) (see inset), which are indicative of shear band activity governing the deformation behaviour of these materials [34, 35].

Table 2 lists the values of the parameters  $H$ ,  $E_r$ ,  $H/E_r$ ,  $H^3/E_r^2$  and  $h_{max}$  for the studied alloys. The hardness increases from 8.46 GPa for  $Cu_{50}Zr_{44}Al_6$  to 10.15 GPa for  $Cu_{56}Zr_{38.7}Al_{5.3}$  alloy while for the intermediate composition (i.e.,  $Cu_{53}Zr_{41.4}Al_{5.6}$ ) the hardness is 9.37 GPa, closer to  $Cu_{56}Zr_{38.7}Al_{5.3}$  than to  $Cu_{50}Zr_{44}Al_6$ . These results are consistent with the XRD scans (Fig. 1) since the degree of crystallinity for  $Cu_{56}Zr_{38.7}Al_{5.3}$  and  $Cu_{53}Zr_{41.4}Al_{5.6}$  alloys is closer to each other than from  $Cu_{50}Zr_{44}Al_6$  alloy. The hardness is larger than those reported for Zr-based metallic glasses [36, 37] and ZrCu-

based metallic glasses [38]. The increase of hardness  $H$  with the Cu content is presumably associated to the brittle and hard  $\text{Cu}_{10}\text{Zr}_7$ ,  $\text{Cu}_8\text{Zr}_3$  intermetallic phases in  $\text{Cu}_{50}\text{Zr}_{44}\text{Al}_6$  since for  $\text{Cu}_{50}\text{Zr}_{50}$  the hardness at 300 mN (using the same experimental setup) was reported to be of only about 6 GPa [39].

The values of maximum displacement also agree with the hardness trend since an increase in hardness involves a lower ability to plastic deformation. Another important listed parameter is the contact modulus  $E_r$ , which gives information about the stiffness of the contact between the sample and the indenter tip. The values increase from 108 to 123 GPa as the content of Cu increases from 50 to 56 at. %. For the intermediate composition, the value of  $E_r$  (i.e., 121 GPa) is closer to that of  $\text{Cu}_{56}\text{Zr}_{38.7}\text{Al}_{5.3}$  than to  $\text{Cu}_{50}\text{Zr}_{44}\text{Al}_6$ , which agrees with the relatively large fraction of crystalline phases in both samples. Nonetheless, this behaviour could also be attributed, at least in part, to differences in the composition since the Young's modulus of Cu (i.e.,  $E_{\text{Cu}}=130$  GPa), is higher than that of Zr and Al ( $E_{\text{Zr}}=68$  GPa,  $E_{\text{Al}}=70$  GPa) [40]. The value of  $E_r$  for  $\text{Cu}_{50}\text{Zr}_{44}\text{Al}_6$  is not far from 112.5 GPa, previously reported for an alloy with similar composition [38]. These materials could also potentially exhibit good tribological performance, given their high  $H$  values and the bright appearance obtained after polishing their surfaces. In order to estimate the wear resistance, the values of  $H/E_r$  [41] and  $H^3/E_r^2$  [42] were assessed since these parameters have been reported to be more representative of the wear resistance than the hardness itself. The parameter  $H/E_r^2$  indicates the resistance to plastic deformation [43] and its dependence with the Cu content correlates well with that of the displacement values  $h_{\text{max}}$  from nanoindentation tests. The values of both  $H/E_r^2$  and  $H^3/E_r^2$  increase with increasing the Cu content.  $H/E_r^2$  increases from 0.078 to 0.082, for  $\text{Cu}_{50}\text{Zr}_{44}\text{Al}_6$  and  $\text{Cu}_{56}\text{Zr}_{38.7}\text{Al}_{5.3}$  alloys, respectively, while  $H^3/E_r^2$  increases from 0.052 to 0.069. These results suggest that the wear resistance of  $\text{Cu}_{50+x}(\text{Zr}_{44}\text{Al}_6)_{50-x}$  alloys should be maximum for the most crystalline composition, i.e.,  $\text{Cu}_{56}\text{Zr}_{38.7}\text{Al}_{5.3}$ . Hence, this behaviour can be associated with the nature and volume fraction of the crystalline phases in each composition. For further assessment of the wear resistance, scratch tests were also performed.

### 3.2.2. Scratch tests

In order to assess the wear behaviour of the different compositions scratch tests were performed at approximately half the radius distance from the centre. It is important to take into consideration that in scratch tests the deformation is more complex than in indentation since the material is not only subjected to a compressive load normal to the surface but simultaneously a shear load is acting parallel to the scratch direction. The temperature rise upon scratching has not been measured but considering the low sliding speed (10 mm/min) and low applied load (30 N) no crystallization is expected [44, 45]. This is especially true for alloys corresponding to the Cu-Zr-Al system since they exhibit high glass transition temperature (above 400°C) [46].

Differences in wear behaviour among the three compositions were analysed from the morphology of the scratches and the cross section profile as shown in Fig. 5. For each composition the pile-up size, groove depth at the centre and the maximum depth, the average ( $R_a$ ) and total roughness

( $R_z$ ) are indicated in the figure. Fig. 5a shows that the scratch for  $\text{Cu}_{50}\text{Zr}_{44}\text{Al}_6$  alloy contains multiple lateral cracks in the pile-up separated at a distance of about 25 to 50  $\mu\text{m}$  from each other. The cracks are relatively short (up to about 50  $\mu\text{m}$ ) and do not seem to propagate beyond the pile-up width. For the  $\text{Cu}_{53}\text{Zr}_{41.4}\text{Al}_{5.6}$  alloy (Fig. 5b) the density of cracks growing from the scratch is much smaller and the distance from each other is larger. In addition, they are not confined to the pile-up but propagate larger distances, up to 150  $\mu\text{m}$ . The largest cracks are detected for the composition  $\text{Cu}_{56}\text{Zr}_{38.7}\text{Al}_{5.3}$  alloy since they extend well beyond 200  $\mu\text{m}$  and the crack density is also larger than for  $\text{Cu}_{53}\text{Zr}_{41.4}\text{Al}_{5.6}$  alloy. Finally, for the composition  $\text{Cu}_{56}\text{Zr}_{38.7}\text{Al}_{5.3}$  (Fig. 5c) the cracks are not only longer (they extend well beyond 200  $\mu\text{m}$ ) but their density is also higher (distance from each other from about 50 to 100  $\mu\text{m}$ ). Moreover, the cracks also propagate towards the inner part of the track as shown in the detail (red square). This feature is similar to the brittle tensile cracking observed by Bull [47] and therefore the results suggest that the composition  $\text{Cu}_{56}\text{Zr}_{38.7}\text{Al}_{5.3}$  is very brittle. From crack analysis it can be clearly observed that the samples embrittle as the Cu content increases.

For each composition, along with the microscopy images, the 2D cross sectional profiles are shown (left panels). The horizontal red line corresponds to the substrate level and it is used as reference to measure the pile-up height (maximum) and groove depth, i.e., the depth of the track at the centre and maximum depth of the track. All these values have been obtained from 5 different measurements at about half the radius distance from the centre. For the  $\text{Cu}_{50}\text{Zr}_{44}\text{Al}_6$  alloy the height of the pile-up is  $4.13 \pm 1.98$   $\mu\text{m}$  while the depth of the groove at the centre and at the maximum depth are  $14.08 \pm 1.20$  and  $22.20 \pm 3.95$ , respectively. However, as the alloy becomes richer in Cu ( $\text{Cu}_{53}\text{Zr}_{41.4}\text{Al}_{5.6}$  composition in Fig. 5b), the height of the pile-up gets smaller and the groove depth at the centre and at the maximum depth increase slightly. The maximum height of the pile-up is only about  $2.65 \pm 1.71$   $\mu\text{m}$  while the depth at the centre and maximum depth reach  $20.10 \pm 7.1$   $\mu\text{m}$  and  $31.1 \pm 7.08$   $\mu\text{m}$ , respectively.

For the alloy with the highest content,  $\text{Cu}_{56}\text{Zr}_{38.7}\text{Al}_{5.3}$  (Fig. 5c), the height of the pile-up decreases slightly to  $2.10 \pm 0.84$   $\mu\text{m}$  while the groove depth at the centre ( $20.00 \pm 2.02$   $\mu\text{m}$ ) and maximum depth ( $31.42 \pm 5.56$   $\mu\text{m}$ ) are very similar to those observed in  $\text{Cu}_{53}\text{Zr}_{41.4}\text{Al}_{5.6}$  alloy. Differences can be also analyzed in terms of scratch groove volume to pile-up volume for the three compositions. The values are 5-6 for  $\text{Cu}_{50}\text{Zr}_{44}\text{Al}_6$ , 15-16 for  $\text{Cu}_{53}\text{Zr}_{41.4}\text{Al}_{5.6}$  and 40-41 for  $\text{Cu}_{56}\text{Zr}_{38.7}\text{Al}_{5.3}$ . These results are consistent with the trend from XRD scans (Fig. 1) and SEM results (Fig. 2), since a small copper increase from 50 to 53 at. % changes the microstructure dramatically while from 53 to 56 at. % Cu microstructural differences are relatively small. However, the pile-up height and groove depth difference for the alloys with highest content of copper are negligible since they are within the error tolerance. The roughness of the groove surface at the track is significant and differences for the three compositions have been analyzed. Fig. 5b and 5c show that the profile is more abrupt than in Fig. 5a due to the local presence of narrow deep pits and suggests that alloys containing 53 and 56 at. % Cu are more prone to adhesive wear upon dry sliding. The last two compositions not only exhibit higher maximum depth than that of  $\text{Cu}_{50}\text{Zr}_{44}\text{Al}_6$  alloy but also, the difference of distance

between the maximum depth and the depth at the centre is  $\sim 11\ \mu\text{m}$  versus  $\sim 8\ \mu\text{m}$  for  $\text{Cu}_{50}\text{Zr}_{44}\text{Al}_6$ , suggesting that the groove is steeper due to the abrasion generated when the intermetallic particles are dragged. In any case, the profiles for the different compositions show common features, i.e., the groove depth at the centre of the track is generally smaller than at both sides probably because the brittle intermetallic particles (abrasive debris) pulled out by the tip tend to slide to both sides of the tip upon scratching and they are afterwards dragged along the track.

To better assess differences of wear mechanism among the three compositions, the morphological features from the track surface have been analyzed in detail (see magnified SEM images of Fig. 6). For each composition representative 2D cross sectional profiles obtained along the track centreline for a distance of  $100\ \mu\text{m}$  are also shown, but SEM images were taken from a smaller and representative distance. The alloy containing 50 at. % Cu (Fig. 6a) exhibits a relatively smooth smeared groove surface without signs of abrasion and consisting of a wavy profile (see inset) with roughness features ranging from a maximum height of  $2\ \mu\text{m}$  to a minimum depth of  $-1\ \mu\text{m}$ . These features suggest ductile plowing and plasticity [48]. As the composition gets richer in Cu, the groove surface tends to turn rougher. For the composition  $\text{Cu}_{53}\text{Zr}_{41.4}\text{Al}_{5.6}$  (Fig. 6b) clear signs of significant detachment outlined by a sharp contour (chipping) (see small arrows) is observed, suggesting that adhesive transfer to the diamond tip has taken place. Small pits of about  $1\ \mu\text{m}$  size are also detected (wider arrow) which could be associated to the pulling out of the intermetallic particles due to adhesion of these particles to the diamond tip upon scratching. These results suggest that the particle-matrix interface is relatively weak. While the dendritic particles exhibit a rough enough contour to remain mechanically attached to the matrix, those particles that exhibit rather rounded shapes can slide and be pulled out more easily.

The cross sectional profile (inset of Fig. 6b) exhibits a more rough pattern with grooves that tend to be deeper than for  $\text{Cu}_{50}\text{Zr}_{44}\text{Al}_6$  alloy (for the representative profile of Fig. 6b the groove can be as deep as  $3\ \mu\text{m}$ ). The large area of transferred particles are smeared across the surface as they are dragged forward by the scratch diamond leading to some surface roughening and adhesive wear. The smaller intermetallic particles are harder and generate abrasive damage as they slide across the surface.

For  $\text{Cu}_{56}\text{Zr}_{38.7}\text{Al}_{5.3}$  alloy (Fig. 6c) signs of detachment (small arrow) and pits (large arrow) are also detected observed but the volume fraction of pits is larger and the surface is more grooved than for the  $\text{Cu}_{53}\text{Zr}_{41.4}\text{Al}_{5.6}$  alloy, which is consistent with the presence of a larger volume fraction of brittle crystalline phases. Additionally, microcracks are observed across the track. There is also evidence for smearing of material along the sample surface in the track. These features suggest that the material has been subjected to adhesive wear, although abrasive wear also takes place as deduced from the grooved surface similarly to that observed in Zr-based BMGs [49].

The roughness of the profile becomes even more prominent with maximum groove depth up to about  $7\ \mu\text{m}$  (see inset). Comparing the amplitude and spacing of the serrations one can observe that they tend to increase with increasing copper content.

It is interesting to observe that the depth of the grooves shown in Fig. 5 is larger for the alloys which are more brittle (highest Cu content). A priori, one might expect that the wear resistance should be higher in the mechanically harder alloys (i.e., Cu-rich), where the track depth should thus be smaller. This is opposite to our observations. This inconsistency with the hardness results (Table 2) can be attributed to the differences in the stress conditions of the material upon indentation and scratching (compression and shear forces). Namely, scratching is more sensitive to the properties of the matrix and the amount (and size) of precipitates, since a softer matrix would easily allow easier dragging of the precipitate particles. For  $\text{Cu}_{56}\text{Zr}_{38.7}\text{Al}_{5.3}$  the size of the crystalline particles (dendrites and rounded particles) is larger, they are very abundant and detach more easily from the matrix than for the alloys depleted in Cu and the precipitate particles tend to detach more easily in this case, causing larger grooves. The complexity of the microstructure for these alloys could explain the co-existence of multiple wear mechanisms.  $\text{Cu}_{50}\text{Zr}_{44}\text{Al}_6$  (i.e., ductile plowing and plasticity detected as a smeared surface),  $\text{Cu}_{53}\text{Zr}_{41.4}\text{Al}_{5.6}$  (i.e., adhesive wear with some abrasive wear and stripping) and  $\text{Cu}_{56}\text{Zr}_{38.7}\text{Al}_{5.3}$  (i.e., highest adhesive wear and highest stripping along with similar abrasive wear to  $\text{Cu}_{53}\text{Zr}_{41.4}\text{Al}_{5.6}$  alloy). As far as the authors are concerned there is a lack of literature available for scratch tests using diamond tip of BMG composites for this alloy system and therefore it is difficult to compare the data.

The percolation threshold for these composites is not far from that of  $\text{Cu}_{53}\text{Zr}_{41.4}\text{Al}_{5.6}$  (~35 vol. %) which could mainly explain the large difference in mechanical performance and wear mechanism between the alloys containing 50 to 53 at. % Cu (Fig. 6a and b). Once the percolation threshold is achieved it is known that the crystalline phases of the material loses its ductility causing an abrupt change in the mechanical properties of the metallic glass [50]. As the critical crystallinity is reached, the viscosity and elastic modulus of the alloys increases suddenly, while the fracture stress, yield strength and ultimate strength are reduced [50, 51]. This effect is in agreement with the results obtained in nanoindentation and scratch tests. As the Cu 53 at. % alloy reaches the percolation threshold, the Young's modulus increases to 121 GPa, in contrast with the 108 GPa obtained in the Cu 50 at. % alloy. However, for 53 and 56 at. % Cu the connectivity between the crystalline phases is not that different as could be inferred from the similar morphology of the track (Fig. 6b and 6c) and the small increase in the reduced Young's modulus (123 GPa). At the same time, the increase in crystalline volume fraction leads to the embrittlement of the material, demonstrated by the appearance of cracks and lower pile up for the 53 and 56 at. % Cu alloys. The embrittlement enhancement when percolation of the crystalline phase takes place suggests that the intermetallic phases are inherently brittle [28].

### 3.3 Wettability and Antimicrobial tests

To assess the potential interest of these alloys for antimicrobial applications not only antimicrobial tests were performed but also the wettability was studied since this provides useful information about the ability for bacterial adhesion on surfaces [52]. The wettability can be analysed by measuring the contact angle of sessile droplets. Fig. 7 shows the average water contact angle on

the three alloys: 101.8° for  $\text{Cu}_{50}\text{Zr}_{44}\text{Al}_6$ , (Fig. 7a), 99.8° for  $\text{Cu}_{53}\text{Zr}_{41.4}\text{Al}_{5.6}$ , (Fig. 7b) and 90.2° for  $\text{Cu}_{56}\text{Zr}_{38.7}\text{Al}_{5.3}$  (Fig. 7c). The angle 101.8° is not far from 106.6° detected in a fully amorphous  $\text{Cu}_{48}\text{Zr}_{42}\text{Ti}_4\text{Al}_6$  at. % metallic glass thin film [53]. The decrease of the contact angle suggests that the material becomes more hydrophilic with increasing Cu content and therefore this should favour the adhesion of bacteria on the surface. This large effect is probably mostly associated with a change in the crystallinity rather than compositional change since similar differences in contact angle are reported when comparing Zr-based and Cu-based metallic glasses [53], i.e., alloys with very different compositions. However, the differences in Cu-content for the Cu-Zr-Al alloys studied here is of only 6 at. %.

The antimicrobial behaviour of the alloys was assessed from reduction in bacterial cells over the time for different initial bacterial densities. When  $2.4 \times 10^8$  bacterial cells were applied to the surface of the samples, there was no reduction observed with sample  $\text{Cu}_{50}\text{Zr}_{44}\text{Al}_6$  when compared to the control samples. After 4 hours of contact with the  $\text{Cu}_{53}\text{Zr}_{41.4}\text{Al}_{5.6}$  sample, *E. coli* and *B. subtilis* numbers were reduced by ca. 50% and 70% respectively. The  $\text{Cu}_{56}\text{Zr}_{38.7}\text{Al}_{5.3}$  sample reduced cell numbers by  $\geq 90\%$  for both species (results not shown). For initial inoculum density of ca.  $1 \times 10^6$  cells/ml, the time-kill curves were obtained for  $\text{Cu}_{53}\text{Zr}_{41.4}\text{Al}_{5.6}$  and  $\text{Cu}_{56}\text{Zr}_{38.7}\text{Al}_{5.3}$  samples up to 250 min (Fig. 8). Both alloys displayed a  $> 3\text{-log}_{10}$  reduction in colony-forming units (cfu)/ml which is consistent with a bactericidal mode of action and with studies investigating bacterial surface contact with copper containing materials [54, 55]. In this study, *E. coli* was less resistant to contact killing than *B. subtilis*. This observation agrees with mode-of-action studies for copper-mediated killing of *E. coli* and *B. subtilis*, as *B. subtilis* produces endospores that are resistant to copper alloy surface killing [56]. The antimicrobial mode of action of copper is described as being reliant on three key properties: 1) copper oxidizes in air of moderate humidity, 2) the copper oxides formed are soluble in the aqueous phase, and 3) the copper ions are toxic to bacteria resulting in damage of intracellular components [57]. The antimicrobial properties of the samples investigated in this study are explained by their differing microstructures: the samples become more crystalline as the copper content increases, which should favour the release of  $\text{Cu}^+$  and  $\text{Cu}^{++}$  cations through easier diffusion paths in crystalline than in amorphous structures. Furthermore, as the copper content increases, the samples become less hydrophobic and therefore the bacteria-surface contact area increases resulting in an improved rate of killing (Fig. 8). The findings in this study suggest that increasing the antimicrobial properties of copper metallic glass composites can be achieved by manipulating the microstructure of the alloy through composition control. Among the three compositions studied, maximum antimicrobial behaviour and wear resistance is attained by the  $\text{Cu}_{56}\text{Zr}_{38.7}\text{Al}_{5.3}$  composition and therefore it could be potentially interesting for the healthcare sector for which optimum performance is desired.

#### 4. Conclusions

In this study, the antimicrobial activity and tribological behaviour of Cu-based BMG composites were investigated. The presence of an increasing content of hard intermetallic phases in the

$\text{Cu}_{53}\text{Zr}_{41.4}\text{Al}_{5.6}$  and  $\text{Cu}_{56}\text{Zr}_{38.7}\text{Al}_{5.3}$  alloys results in an increasing embrittlement of the  $\text{Cu}_{50}\text{Zr}_{44}\text{Al}_6$  alloy. This is suggested by the cracks, lower pile-up, prone adhesion wear in dry sliding and higher scratch groove volume to pile-up volume revealed in the scratch test. The wear resistance also increases with increasing Cu content as indirectly assessed from  $H/E_r$  and  $H^3/E_r^2$  parameters. The results from the sessile drop technique show lower contact angle values with increasing Cu content, which favours adhesion of bacteria to the substrate. The  $\text{Cu}_{56}\text{Zr}_{38.7}\text{Al}_{5.3}$  alloy shows improved increase in contact killing for *B. Subtilis* and *E. Coli* during the first hour of interaction, which can be useful to prevent bacteria spreading on touch surfaces.

## 5. Acknowledgments

V.M.V. and S.G. acknowledge research support from Northumbria University. Partial financial support from 2014-SGR-1015 (Generalitat de Catalunya), and MAT2014-57960-C3-1-R (from MINECO, co-financed by FEDER) is acknowledged. We acknowledge G. Wells and the Smart Materials and Surfaces Laboratory from Northumbria University for the support with the sessile drop tests.

## References

- [1] G. Sorci, S. Cornet, B. Faivre, Immunity and the emergence of virulent pathogens. *Infection. Genetics and Evolution* 16 (2013) 441-446.
- [2] J.A.Trubiano, A.A. Padiglione, Nosocomial infections in the intensive care unit. *Anaesthesia and Intensive Care. Medicine* 16 (2015) 2068-2077.
- [3] H. Sadatsafavi, B. Niknejad, R. Zadeh, M. Sadatsafavi, Do cost savings from reductions in nosocomial infections justify additional costs of single-bed rooms in intensive care units? A simulation case study. *Journal of Critical Care* 31 (2015) 1-22.
- [4] S. Lax, J.A. Gilbert, Hospital associated microbiota and implications for nosocomial infections. *Cell Press* 21 (2015) 427-432.
- [5] European Centre for Disease Prevention and Control (2013). Point prevalence survey of healthcare associated infections and antimicrobial use in European acute care hospitals. Stockholm, ECDC.
- [6] C.E. Santo, E.W. Lam, C.G. Elowsky, D. Quaranta, D.W. Domaille, C.J. Chang, G. Grass, Bacterial killing by dry metallic copper surfaces. *Applied and Environmental Microbiology* 77 (2011) 794-802.
- [7] J. Qiao, H. Jia, P.K. Liaw, Metallic glass matrix composites. *Material Science and Engineering R* 100 (2016) 1-69.
- [8] T. Gloriant, Microhardness and abrasive wear resistance of metallic glasses and nanostructured composite materials. *Journal of non-crystalline solids* 316 (2003) 96-103.
- [9] J. Bhatt, S. Kumar, C. Dong, B.S. Murty, Tribological behaviour of Cu<sub>60</sub>Zr<sub>30</sub>Ti<sub>10</sub> bulk metallic glass. *Materials Science and Engineering* 458 (2007) 290-294.
- [10] L. Huang, E.M. Fozo, T. Zhang, P.K. Liaw, W. He, Antimicrobial behaviour of Cu-bearing Zr-based bulk metallic glasses. *Materials Science and Engineering C* 39 (2014) 325-329.
- [11] C.Y. Tam, C.H. Shek, E. Fleury, S.M. Lee, H.S. Ahn, W.T. Kim, D.H. Kim, Tribological properties of bulk metallic glasses. *Materials Science and Engineering: A*. 375(2004) 276-279.
- [12] M. Bakkal, Sliding tribological characteristics of Zr-based bulk metallic glass under lubricated conditions. *Intermetallics* 18 (2010) 1251-1253.
- [13] Y. Wang, L. Zhang, T. Wang, X.D. Hui, W.Chen, C.F. Feng, Effect of sliding velocity on the transition of wear mechanism in (Zr,Cu)<sub>95</sub>Al<sub>5</sub> bulk metallic glass. *Tribology International* 101 (2016) 141-151.
- [14] C.W. Chu, J.S. Jang, G.J. Chen, S.M. Chiu, Characteristic studies on the Zr-based metallic glass thin film fabricated by magnetron sputtering process. *Surface and Coatings Technology* 202 (2008) 5564-5566.
- [15] A. Inoue, Stabilization of metallic supercooled liquid and bulk amorphous alloys. *Acta Materialia* 48 (2000) 279-306.
- [16] V.K. Champagne, D.J. Helfrich, Ademonstration of the antimicrobial effectiveness of various copper surfaces. *Journal of Biological Engineering* 7 (2013) 1-6.



- [17] Y.C. Kim, J.C. Lee, P.R. Cha, J.P. Ahn, E. Fleury, Enhanced glass forming ability and mechanical properties of new Cu-based bulk metallic glasses. *Materials Science and Engineering A* 437 (2006) 248-253.
- [18] Q. Wang, Y.M. Wang, J.B. Qiang, X.F. Zhang, C.H. Shek, C. Dong, Composition optimization of the Cu-based CuZr-Al alloys. *Intermetallics* 12 (2004) 1229-1232.
- [19] P. Yu, H.Y. Bai, Poisson's ratio and plasticity in CuZrAl bulk metallic glasses. *Material Science and Engineering A* 485 (2008) 1-4.
- [20] T.J. Meyer, J. Ramdall, P. Thu, N. Gadura, Antimicrobial properties of copper in gram-negative and gram-positive bacteria. *Int. Journal of Biological, Biomolecular, Agricultural, Food and Biotechnological Engineering* 9 (2015) 274-278.
- [21] J.H. Chu, J. Lee, C.C. Chang, Y.C. Chan, M.L. Liou, J.W. Lee, J.S.C. Jang, J.G. Duh, Antimicrobial characteristics in Cu-containing Zr-based thin film metallic glass. *Surface and Coatings Technology* 259(2014) 87–93.
- [22] S. Pauly, G. Liu, G. Wang, U. Kühn, N. Mattern, J. Eckert, Microstructural heterogeneities governing the deformation of Cu<sub>47.5</sub>Zr<sub>47.5</sub>Al<sub>5</sub> bulk metallic glass composites. *Acta Materialia* 57 (2009) 5445-5453.
- [23] S. Gonzalez, Role of minor additions on metallic glasses and composites. *Journal of Material Research* 31 (2016) 76-87.
- [24] D. Wang, Y. Li, B.B. Sun, M. L. Sui, K. Lu, E. Ma, Bulk metallic glass formation in the binary Cu–Zr system. *Applied Physics Letters* 84 (2004) 4029-4031.
- [25] M. Iqbal, W. H. Wang (2014). Production and properties of high strength Ni free Zr-based BMGs. *IOP Conf. Series: Materials Science and Engineering* 60.
- [26] F.R. Boer, R. Boom, W.C.M. Matterns, A.R. Miedema, A.K. Niessen *Cohesion in Metals*. Place, 1988.
- [27] S. González, J. Sort, D.V. Louzguine-Luzgin, J.H. Perepezko, M.D. Baró, A. Inoue, Tuning the microstructure and mechanical properties of Al-based amorphous/crystalline composites by addition of Pd. *Intermetallics* 18 (2010) 2377-2384.
- [28] X.L. Fu, Y. Li, C.A. Schuh, Mechanical properties of metallic glass matrix composites: Effects of reinforcement character and connectivity. *Scripta Materialia* 56 (2007) 617-620.
- [29] L. Tretyachenko, Aluminium-Copper-Zirconium, in: G. Effenberg and S. Ilyenko (Eds.), *Light Metal Systems*. Part 2. Springer Place, 2005, 1-17.
- [30] T.S. Srivatsan, T.S. Sudarshan, *Rapid Solidification technology. An engineering guide*. Technomic Publishing Company Place, 1993.
- [31] Y. Yokoyama, H. Inoue, K. Fukaura, A. Inoue, Relationship between the liquidus surface and structures of Zr-Cu-Al bulk amorphous alloys. *Materials Transactions* 43 (2002) 575-579.
- [32] J. Meija, T.B. Coplen, M. Berglund, W.A. Brand, P. De Bièvre, M. Gröning, N.E. Holden, J. Irrgeher, R.D. Loss, T. Walczyk, T. Prohaska, *Atomic weights of the Elements 2013*. *Pure and Applied Chemistry* 88 (2016) 265-291.

- [33] M.W. Chen, Mechanical behaviour of Metallic Glasses: Microscopic Understanding of Strength and Ductility. *Annual Review of Materials Research* 38 (2008) 445-469.
- [34] C.A. Schuh, T.C. Hufnagel, U. Ramamurty, Mechanical behaviour of amorphous alloys. *Acta Materialia* 55 (2007) 4067-4109.
- [35] J. Fornell, A. Concustell, S. Suriñach, W.H. Li, N. Cuadrado, A. Gebert, M.D. Baró, J. Sort, Yielding and intrinsic plasticity of Ti-Zr-Ni-Cu-Be bulk metallic glass. *International Journal of Plasticity* 25 (2009) 1540-1559.
- [36] S. González, E. Pellicer, S. Suriñach, M.D. Baró, J. Sort, Mechanical and corrosion behaviour of as-cast and annealed Zr<sub>60</sub>Cu<sub>20</sub>Al<sub>10</sub>Fe<sub>5</sub>Ti<sub>5</sub>. *Intermetallics* 28 (2012) 149-155.
- [37] S. González, E. Pellicer, S. Suriñach, M.D. Baró, E. García-Lecina, J. Sort, Effect of thermally-induced surface oxidation on the mechanical properties and corrosion resistance of Z60. *Science of Advanced Materials* 6 (2014) 27-36.
- [38] S. González, P. Pérez, E. Rossinyol, S. Suriñach, M.D. Baró, E. Pellicer, J. Sort, Drastic influence of minor Fe or Co additions on the glass forming ability, martensitic transformation and mechanical properties of shape memory Zr-Cu-Al bulk metallic glass composites. *Science and Technology of Advanced Materials* 15 (2016) 035015.
- [39] J. Fornell, M.D. Baró, S. Suriñach, A. Gebbert, J. Sort., The influence of deformation-induced martensitic transformations on the mechanical properties of nanocomposite Cu-Zr-(Al) systems. *Advanced Engineering Materials* 13 (2011) 57-63.
- [40] G.V. Samsonov, *Handbook of the physicochemical properties of the elements*. IFI-Plenum, Place, 1968.
- [41] A. Leyland, A. Matthews, On the significance of the H/E ratio in wear control: a nanocomposite coating approach to optimised tribological behaviour. *Wear* 246 (2000) 1-11.
- [42] J. Musil, F. Kunc, H. Zeman, H. Poláková, Relationships between hardness, Young's modulus and elastic recovery in hard nanocomposite coatings. *Surface and Coating Technology* 154 (2002) 304-313.
- [43] D.L. Joslin, W.C. Oliver, A new method for analyzing data from continuous depth-sensing microindentation tests. *Journal of Materials Research* 5 (1990) 123-126.
- [44] Z. Parlar, M. Bakkal, A.J. Shih, Sliding tribological characteristics of Zr-based metallic glass. *Intermetallics* 16 (2008) 34-41.
- [45] Y. Huijun, L. Yong, Z. Teng, W. Hengpen, T. Bin, Q. Junwei, Dry Sliding Tribological Properties of a Dendrite-reinforced Zr-based Bulk Metallic Glass Matrix Composite. *Journal of Materials Science & Technology* 30 (2014) 576-583.
- [46] A. Inoue, W. Zhang, Formation, thermal stability and mechanical properties of Cu-Zr-Al bulk glassy alloys. *Materials Transactions* 43 (2002) 2921-2925.
- [47] S.J. Bull, Failure mode maps in the thin film scratch adhesion test. *Tribology International* 30 (1997) 491-498.

- [48] F.X. Liu, F.Q. Yang, Y.F. Gao, W.H. Jiang, Y.F. Guan, P.D. Rack, O. Sergic, P.K. Liaw, Micro-scratch study of a magnetron-sputtered Zr-based metallic-glass film. *Surface & Coating Technology* 203 (2009) 3480-3484.
- [49] H. Zhong, J. Chen, L. Dai, Y. Yue, Z. Zhang, X. Zhang, M. Ma, R. Liu, Tribological behaviours of Zr-based bulk metallic glass versus Zr-based bulk metallic glass under relative heavy loads. *Intermetallics* 65 (2015) 88-93.
- [50] J. Basu, N. Nagendra, Y. Li, U. Ramamurty, Microstructure and mechanical properties of a partially crystallized La-based bulk metallic glass. *Philosophical magazine* 83 (2003) 1747-1760.
- [51] Z.Q. Liu, G. Liu, R.T. Qu, Z.F. Zhang, S.J. Wu, T. Zhang, Microstructural percolation assisted breakthrough of trade-off between strength and ductility in CuZr-based metallic glass composites. *Scientific Reports* 4 (2014) 1-6.
- [52] L.K. Ista, S. Mendez, G.P. Lopez, Attachment and detachment of bacteria on surfaces with tunable and switchable wettability. *Biofouling* 26 (2010) 111-118.
- [53] J.P. Chu, T.-Y. Liu, C.-L. Li, C.-H. Wang, J.S.C. Jang, M.-J. Chen, S.-H. Chang, W.-C. Huang, Fabrication and characterization of thin film metallic glasses: Antibacterial property and durability study for medical application. *Thin Solid Film* 561 (2014) 102-107.
- [54] S. Mathews, R. Kumar, M. Solioz, S. Mathews, R. Kumar, M. Solioz, Copper Reduction and Contact Killing of Bacteria by Iron Surfaces. *Applied and Environmental Microbiology* 81 (2015) 6399-6403.
- [55] M.K. Ballo, S. Rtimi, S. Mancini, J. Kiwi, C. Pulgarin, J.M. Entenza, A. Bizzini, Bactericidal activity and mechanism of action of copper-sputtered flexible surfaces against multidrug-resistant pathogens. *Applied microbiology and biotechnology* 100 (2016) 5945-5943.
- [56] K. San, J. Long, C.A. Michels, N. Gadura, Antimicrobial copper alloy surfaces are effective against vegetative but not sporulated cells of gram-positive *Bacillus subtilis*. *Microbiologyopen* 4 (2015) 753-763.
- [57] M. Hans, S. Mathews, F. Mucklich, M. Solioz, Physicochemical properties of copper important for its antibacterial activity and development of a unified model. *Biointerphases* 11 (2016) 018902.

**Figures captions**

Fig. 1. XRD scans for samples (a)  $\text{Cu}_{50}\text{Zr}_{44}\text{Al}_6$  (b)  $\text{Cu}_{53}\text{Zr}_{41.4}\text{Al}_{5.6}$  and (c)  $\text{Cu}_{56}\text{Zr}_{38.7}\text{Al}_{5.3}$  alloys.

Fig. 2. Backscattered SEM images taken from the middle radius for a)  $\text{Cu}_{50}\text{Zr}_{44}\text{Al}_6$ , (b)  $\text{Cu}_{53}\text{Zr}_{41.4}\text{Al}_{5.6}$  and (c)  $\text{Cu}_{56}\text{Zr}_{38.7}\text{Al}_{5.3}$  alloys.

Fig. 3. Magnified backscattered SEM images taken from the middle radius for a)  $\text{Cu}_{50}\text{Zr}_{44}\text{Al}_6$ , (b)  $\text{Cu}_{53}\text{Zr}_{41.4}\text{Al}_{5.6}$  and (c)  $\text{Cu}_{56}\text{Zr}_{38.7}\text{Al}_{5.3}$  alloys.

Table 1. Composition in at. % of the areas labelled on Fig. 3 and phases to which they can be attributed.

Fig. 4. Load-displacement (P-h) nanoindentation curves for a)  $\text{Cu}_{50}\text{Zr}_{44}\text{Al}_6$  (b)  $\text{Cu}_{53}\text{Zr}_{41.4}\text{Al}_{5.6}$  and (c)  $\text{Cu}_{56}\text{Zr}_{38.7}\text{Al}_{5.3}$  alloys.

Table 2. Summary of the mechanical properties of the  $\text{Cu}_{50}\text{Zr}_{44}\text{Al}_6$ ,  $\text{Cu}_{53}\text{Zr}_{41.4}\text{Al}_{5.6}$  and  $\text{Cu}_{56}\text{Zr}_{38.7}\text{Al}_{5.3}$  alloys after nanoindentation using a maximum load of 300 mN. The values of hardness (H), reduced Young's modulus ( $E_r$ ),  $H/E_r$ ,  $H^3/E_r^2$  ratios and maximum indentation depth ( $h_{\max}$ ) are given in the table.

Fig. 5. Images showing the scratches at the middle radius of the samples a)  $\text{Cu}_{50}\text{Zr}_{44}\text{Al}_6$  (b)  $\text{Cu}_{53}\text{Zr}_{41.4}\text{Al}_{5.6}$  and (c)  $\text{Cu}_{56}\text{Zr}_{38.7}\text{Al}_{5.3}$  alloys along with their corresponding 2D cross sectional profiles and numerical values.

Fig. 6. Images showing the central area of the scratches at the middle radius of the samples a)  $\text{Cu}_{50}\text{Zr}_{44}\text{Al}_6$  (b)  $\text{Cu}_{53}\text{Zr}_{41.4}\text{Al}_{5.6}$  and (c)  $\text{Cu}_{56}\text{Zr}_{38.7}\text{Al}_{5.3}$  alloys along with their corresponding 2D cross sectional profiles and numerical values.

Fig. 7. Average water contact angle on Cu-Zr-Al alloys (a, b and c).

Fig. 8. Time-kill curve of *E. coli* K12 and *B. subtilis* 168 exposed to Cu-Zr-Al alloys for up to 250 min.

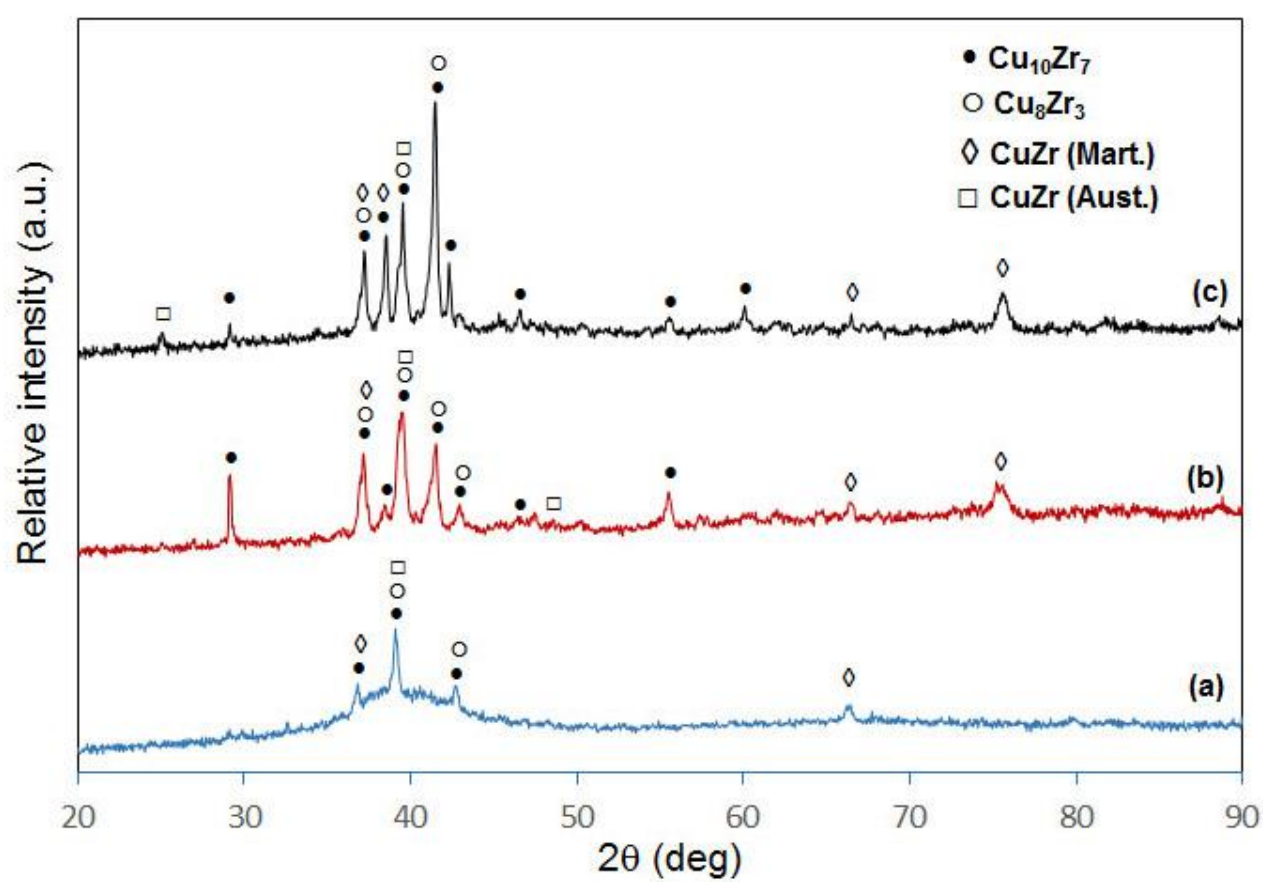


Fig. 1

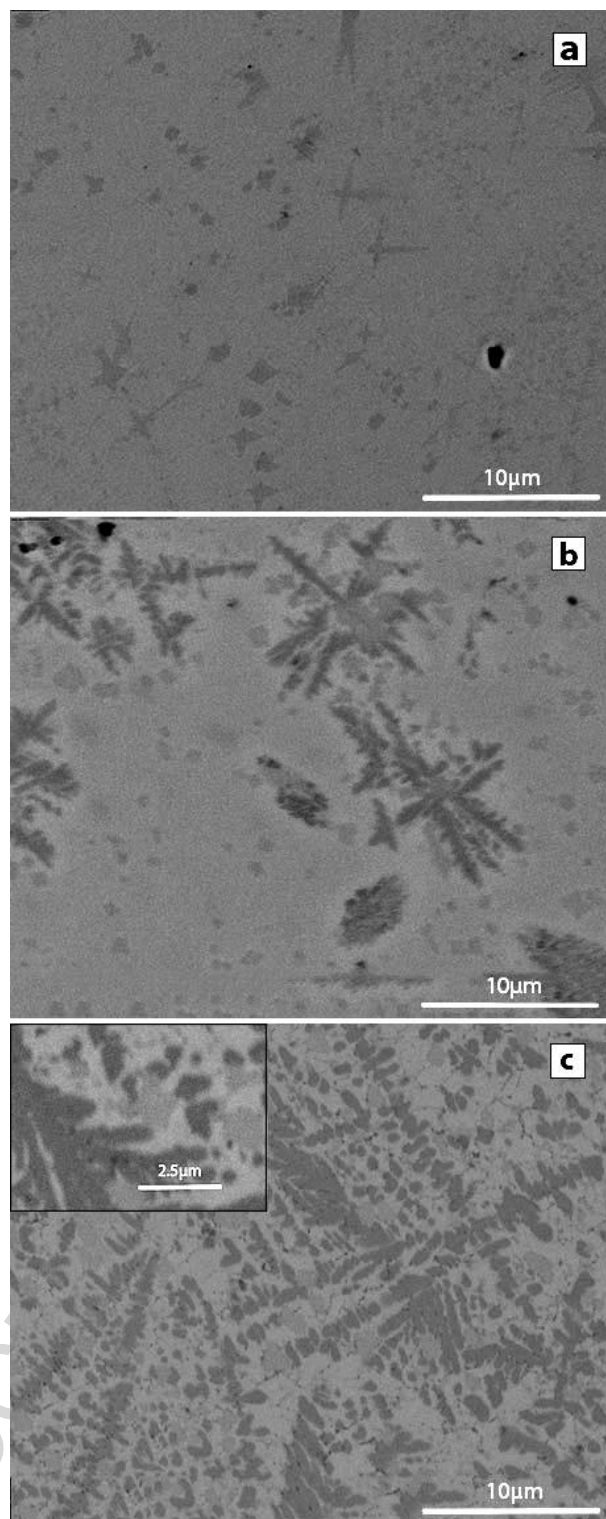


Fig. 2

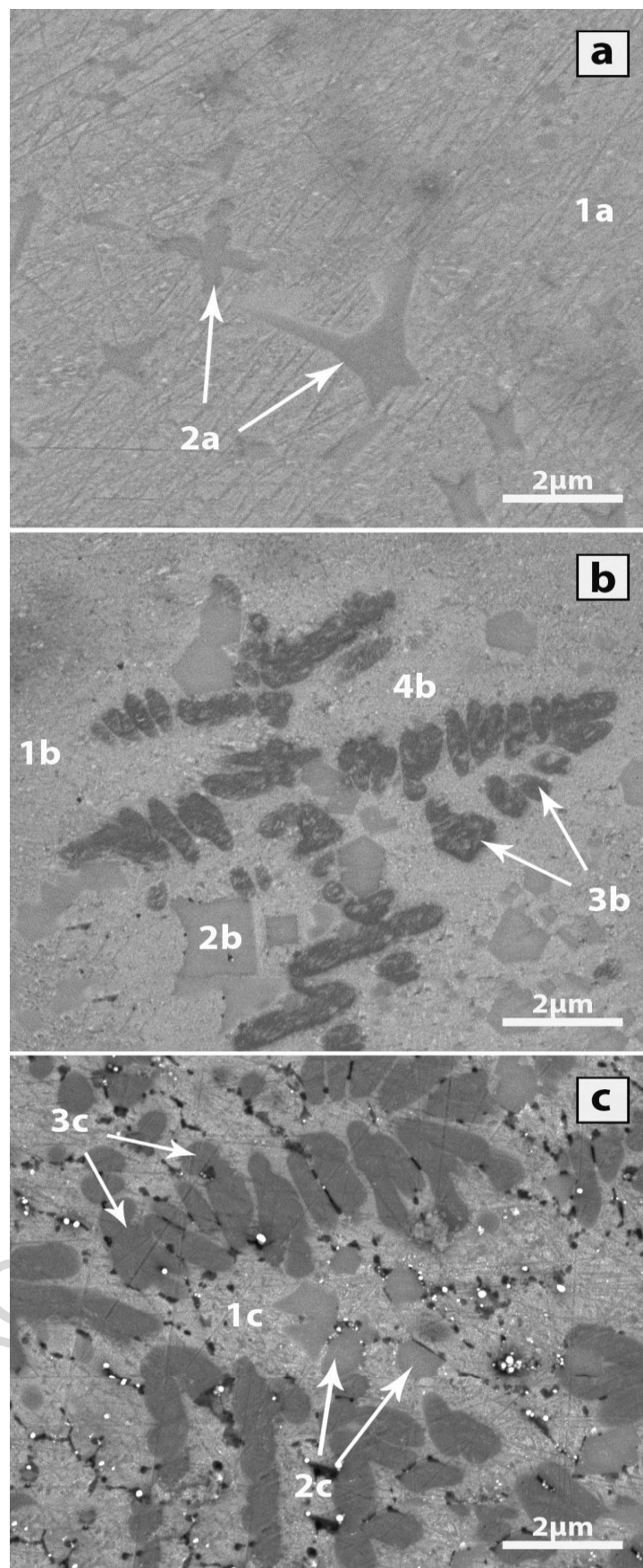


Fig. 3

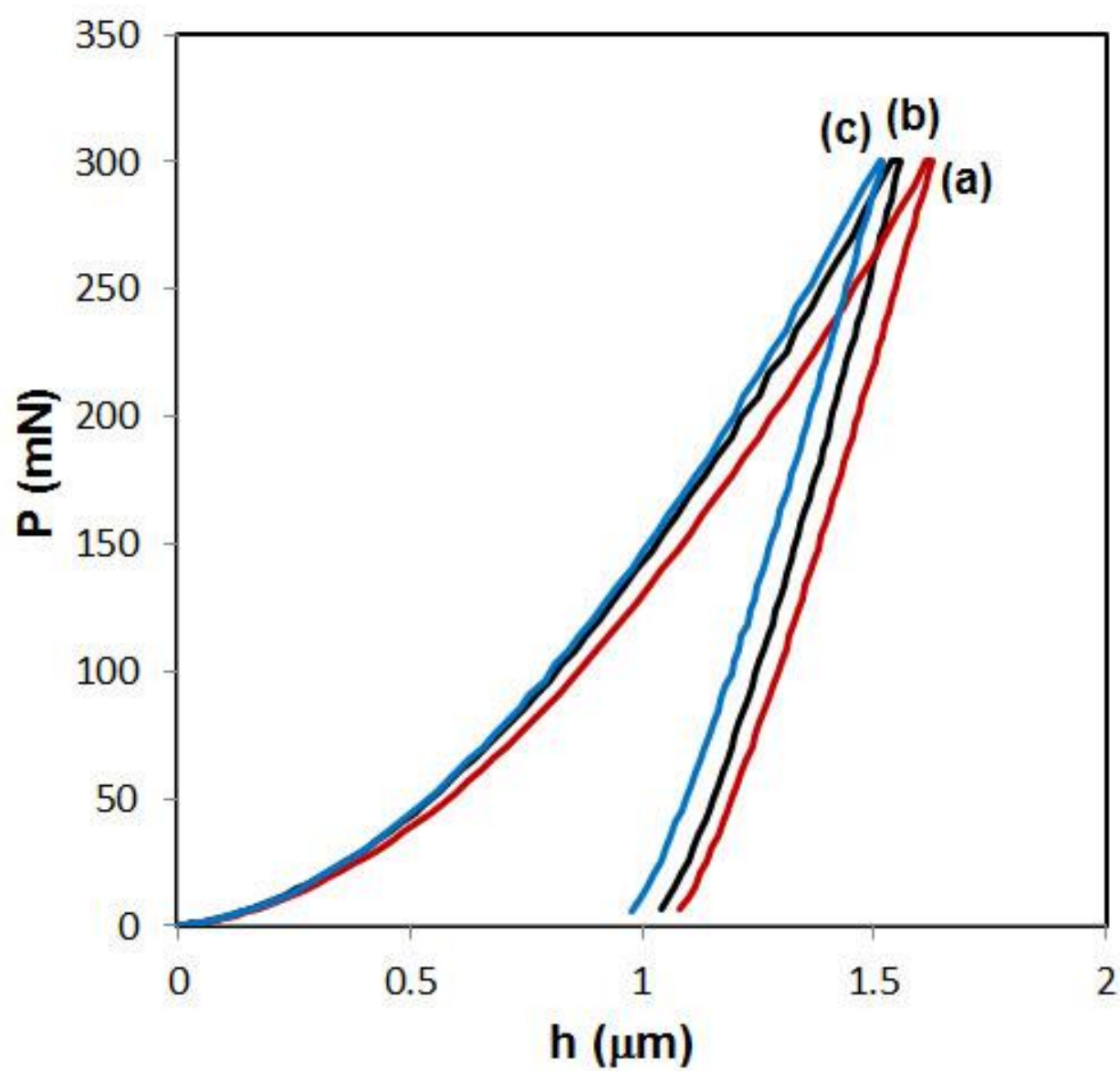


Fig. 4



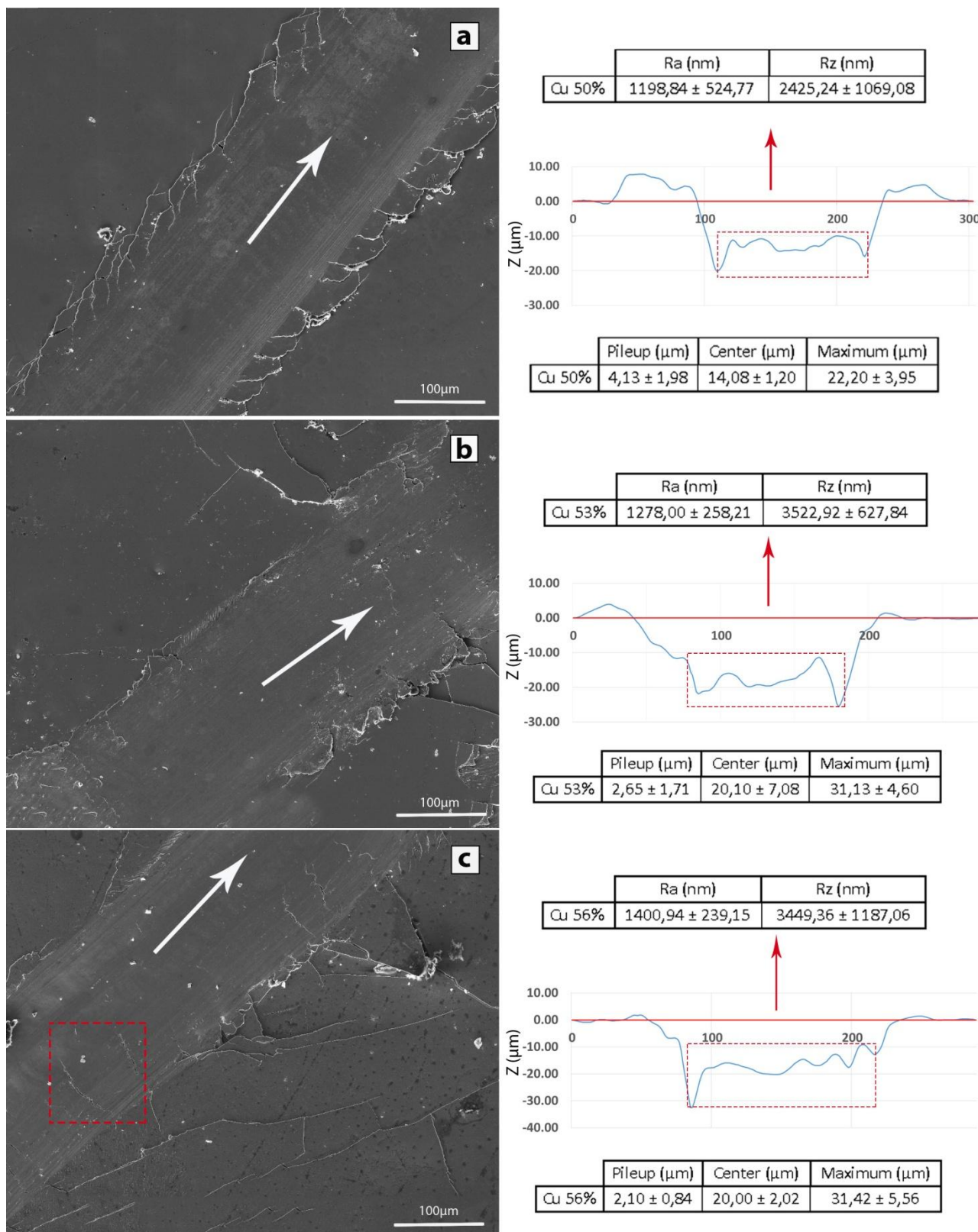


Fig. 5

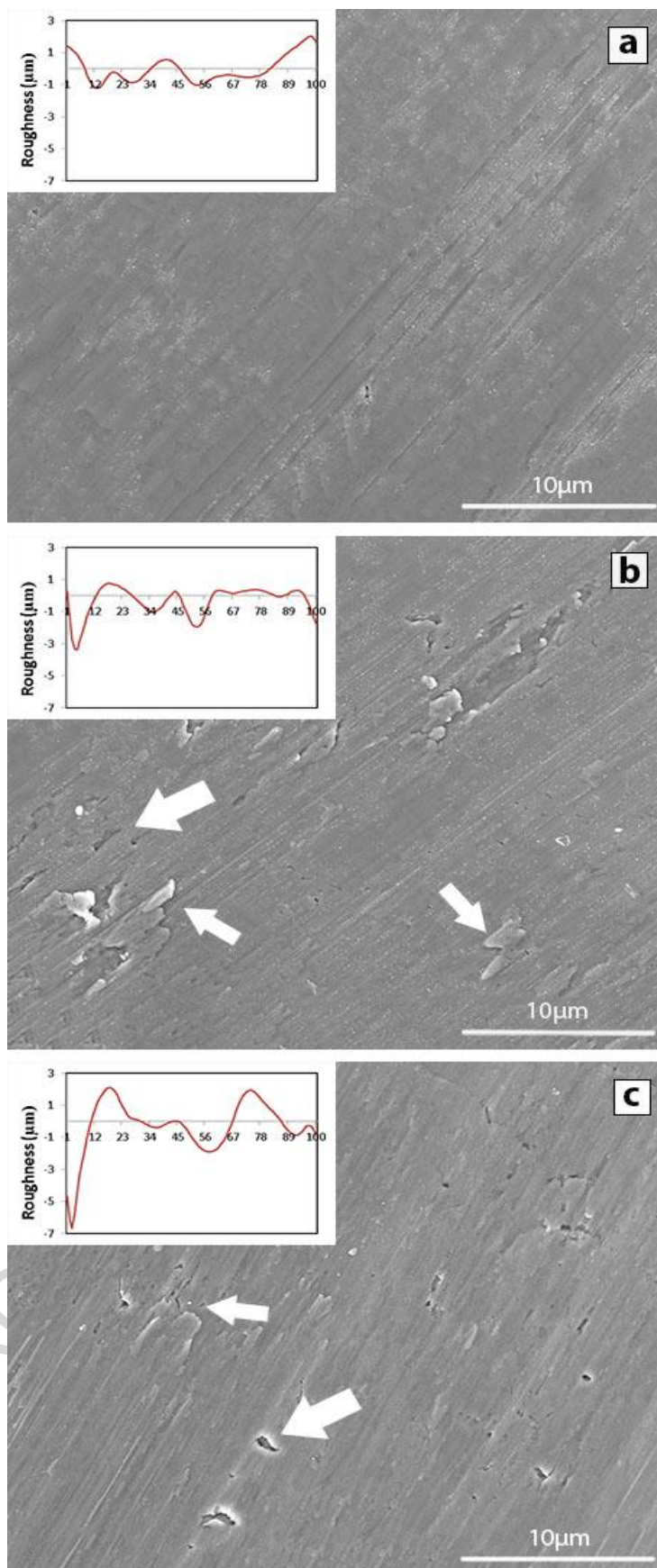


Fig. 6

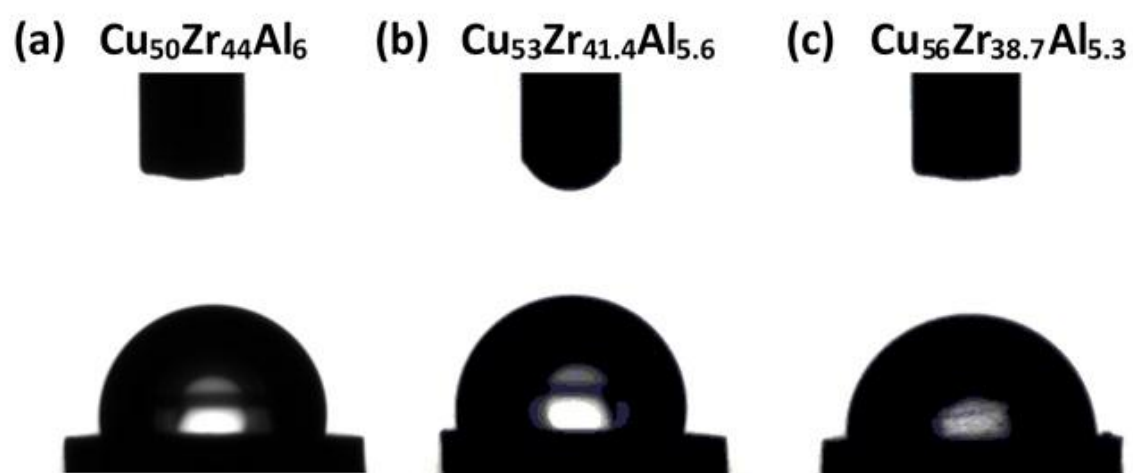


Fig. 7

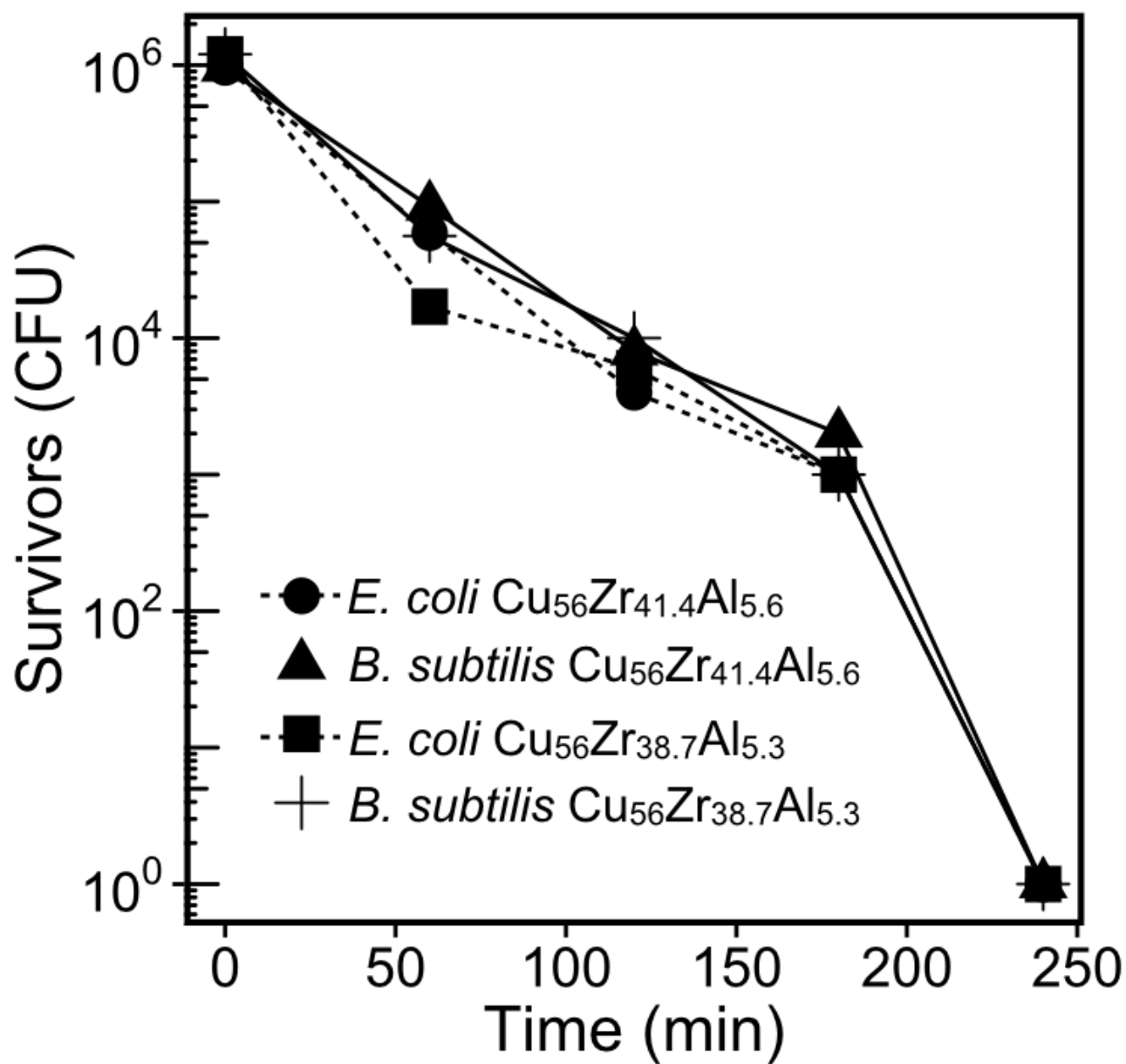


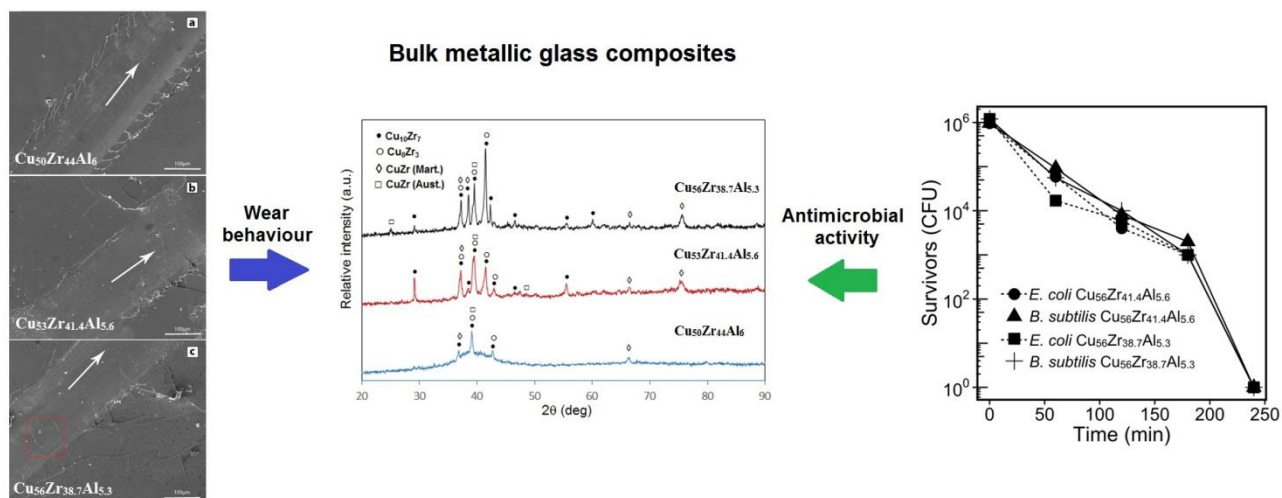
Fig. 8

Table 1

	1a Matrix	1b Matrix	1c Halo	2a Large Dendrites	2b Geometric particles	2c Geometric particles	3b Dendrites	3c Dendrites	4b Halo
Cu	54.3±0.3	55.0±0.6	55.3±0.7	50.2±0.8	42.5±3.0	39.6±1.8	58.7±3.0	61.2±1.2	53.5±1.0
Zr	40.0±0.3	39.3±1.2	42.3±0.7	35.4±1.3	46.2±2.8	48.1±1.3	32.5±3.3	28.3±1.1	42.7±0.8
Al	5.6±0.3	5.7±0.7	2.4±0.4	14.5±0.5	11.3±1.3	12.3±0.6	8.8±0.5	10.5±0.2	3.9±0.7
Phase	Nominal composition	Nominal composition	Cu <sub>10</sub> Zr <sub>7</sub>	Cu <sub>10</sub> Zr <sub>7</sub>	CuZr	CuZr	Cu <sub>8</sub> Zr <sub>3</sub> +Cu <sub>10</sub> Zr <sub>7</sub>	Cu <sub>8</sub> Zr <sub>3</sub>	Cu <sub>10</sub> Zr <sub>7</sub>

Table 2

Property	$\text{Cu}_{50}\text{Zr}_{44}\text{Al}_6$	$\text{Cu}_{53}\text{Zr}_{41.4}\text{Al}_{5.6}$	$\text{Cu}_{56}\text{Zr}_{38.7}\text{Al}_{5.3}$
$H(\text{GPa})$	$8.46 \pm 0.45$	$9.37 \pm 0.28$	$10.15 \pm 1.87$
$E_r(\text{GPa})$	$107.96 \pm 3.57$	$121.19 \pm 1.87$	$123.36 \pm 6.89$
$H/E_r$	$0.078 \pm 0.007$	$0.077 \pm 0.003$	$0.082 \pm 0.020$
$H^3/E_r^2(\text{GPa})$	$0.052 \pm 0.006$	$0.056 \pm 0.007$	$0.069 \pm 0.046$
$h_{\max}(\mu\text{m})$	$1.485 \pm 0.035$	$1.403 \pm 0.017$	$1.372 \pm 0.081$



Graphical abstract

**Highlights**

- The wear resistance increases with the addition of copper from 50 to 56 at. %.
- The contact angle values decrease with increasing Cu content.
- Maximum antimicrobial behaviour and wear resistance is attained by the  $\text{Cu}_{56}\text{Zr}_{38.7}\text{Al}_{5.3}$  composition.

ACCEPTED MANUSCRIPT